Polysilicon Grating Switches for LiDAR

Eugene H. Cook, Steven J. Spector, Michael G. Moebius, Frederick A. Baruffi, Mirela G. Bancu, Lucas D. Benney, Steven J. Byrnes, Jordan P. Chesin, Sarah J. Geiger, Daniel A. Goldman, *Member, IEEE*, Alva E. Hare, Benjamin F. Lane, William D. Sawyer, and Chris R. Bessette

***Abstract*— Novel polysilicon grating switches are demonstrated, consisting of an optical grating suspended on a moving platform above a waveguide. Electrostatic attraction pulls the grating into close proximity to the waveguide, ejecting light out of the waveguide plane. The switches move only 0.9 to 1.4 μm, and have MHz mechanical resonant frequencies, making them robust to mechanical vibration and shock. These switches enable a new mode of LiDAR imaging; by creating a focal plane array of switches, and coupling it with a standard camera lens, the LiDAR beam can be scanned across the scene with high speed and arbitrary pattern. Both time of flight and coherent ranging techniques are compatible with this approach. We have demonstrated a 10 x 10 pixel array of these switches in a LiDAR system, collecting 3D raging data at up to 15 meters away and 5 frames per second, over a 1 degree field of view with 0.1 degree resolution. Additionally, we have shown the switches to be robust, efficient, and reliable, actuating at 15 Volts, with speeds faster than 4 μs, for over 9 billion cycles without degradation or failure. [2020-0132]**

***Index Terms*— MEMS, MOEMS, switch, LiDAR, grating, micro optics, photonics.**

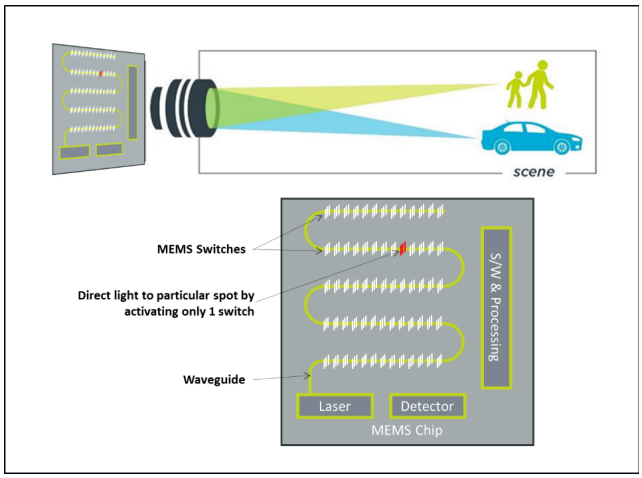

Fig. 1. Example LiDAR architecture. The micro-opto-mechanical chip is placed at the focal plane. Activating one pixel at a time enables the beam to be directed at any point in the scene.

I. Introduction

LiDAR is seen as a key enabling sensor component for autonomous vehicles [1], [2]. LiDAR provides an important tool for high-resolution three-dimensional imaging, with superior resolution to radar and superior range to ultrasonic sensors. Many current autonomous vehicle development platforms rely on traditional LiDAR systems, which use mechanical systems to sweep a laser beam over the scene. For wide deployment in the automotive market, it will be necessary to realize similar LiDAR performance at small cost and size.

A variety of approaches have been developed to enable chip-scale LiDAR components. Optical phased arrays [3], [4] use multiple emitters of controlled phase to electronically steer the light beam within the scene. These have the advantage of very small size and pure solid-state operation, but they rely on complicated analog control of many phase shifters and have difficulty scaling to large arrays. Flash LiDAR [5] simultaneously illuminates the entire scene, and uses an array of detectors to measure returns from each point. However, it requires expensive detector arrays, and can have difficulty keeping the power output within eye-safe limits. MEMS mirrors have also been developed in a number of configurations [6], to mechanically scan the LiDAR beam over the scene. These mirrors also require precision analog position control, typically employ a fixed scan pattern taking advantage of the mechanical resonance, and can be sensitive to vibration and shock because of the suspended flexible structure. Additionally, the design must manage the trade-off between a large mirror to maximize light collection, and a small mirror for fast operation and high resonant frequency, which helps resist vibration.

Another technique is to use a waveguide-based photonic integrated circuit (PIC), with emission gratings, to selectively eject light from individual pixels connected to the waveguide. These pixel arrays, placed in the focal plane of a camera, allow a LiDAR beam to be scanned across a scene by sequentially activating each pixel (Fig. 1). Optics similar to those of an ordinary camera project the beam into the scene. One way to switch light within the waveguide network towards the emission gratings is with Mach-Zehnder Interferometers [7], [8]. However, this approach requires analog control, relatively high power, and can have switching speed limitations. MEMS optical switches that can selectively connect waveguide segments have also been demonstrated [9], [10]. These can actuate quickly, and have much higher mechanical resonant

Manuscript received May 5, 2020; revised June 2, 2020; accepted June 11, 2020. Date of publication June 30, 2020; date of current version October 7, 2020. Subject Editor M. Rais-Zadeh. *(Corresponding author: Eugene H. Cook.)*

The authors are with the Charles Stark Draper Laboratory, Cambridge, MA 02139 USA (e-mail: ecook@draper.com).

Color versions of one or more of the figures in this article are available online at http://ieeexplore.ieee.org.

Digital Object Identifier 10.1109/JMEMS.2020.3004069

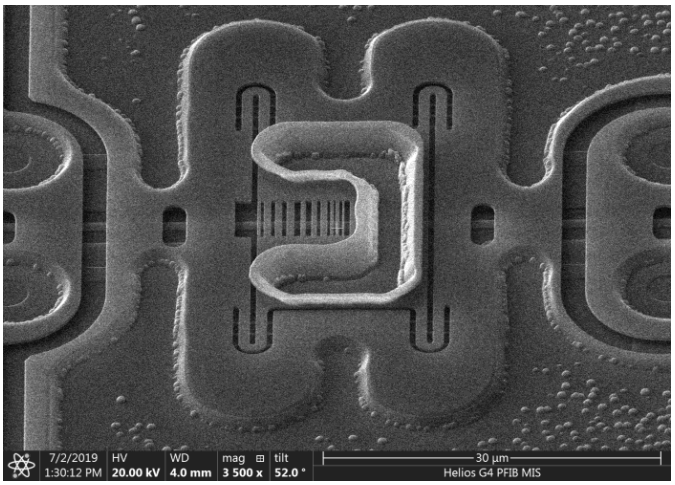

Fig. 2. A SEM shows the grating switch with stiffener. The waveguide is oriented horizontally, under the center of the device. Flexures support the four corners, and the circular features on the sides are electrical routing vias.

frequencies than larger MEMS mirrors, rendering them robust against vibration. In order to improve compactness, we have combined the emission grating and the MEMS switch into one element, rather than using a larger waveguide switch.

Our novel surface micromachined optical switch is presented (Fig. 2). These switches differ from other optical waveguide MEMS switches [9], [10] in that they couple into free space, rather than another waveguide. The switch consists of an optical grating on a moving structure suspended above a waveguide. When "OFF" (no voltage applied), the switch is far enough from the waveguide that light propagating therein does not interact with the grating. When voltage is applied and the switch is "ON" (pulled down), the evanescent field of the light couples to the grating, and the optical design is such that the light is ejected into free space with an engineered emission angle and numerical aperture.

We have also built a LiDAR imager based on these switches [11]. The demonstrated LiDAR system was configured in a bistatic arrangement, with separate lens and single detector element as the receiver. The use of separate chip for the receiver is well suited for the direct time-of-flight range measurements. Other LiDAR system configurations, such as using the same grating or an adjacent grating in the receiver are also possible, and are well suited to coherent approaches to measure the range from the reflected signal.

II. Fabrication

The fabrication process (Fig. 3) begins with a thermal oxide lower cladding, which prevents optical coupling to the silicon substrate. Polysilicon is then deposited, implanted with boron, annealed and patterned, forming the lower electrodes which attract the switch into the "ON" position. LPCVD nitride is deposited. The nitride waveguides provide low loss (measured at about 7 dB/cm) while still resisting HF during the release.

The nitride is patterned twice. First the waveguide is etched. Dimples (200 nm diameter circles and 200 nm bars) are also etched in the nitride, on top of the electrode and under the

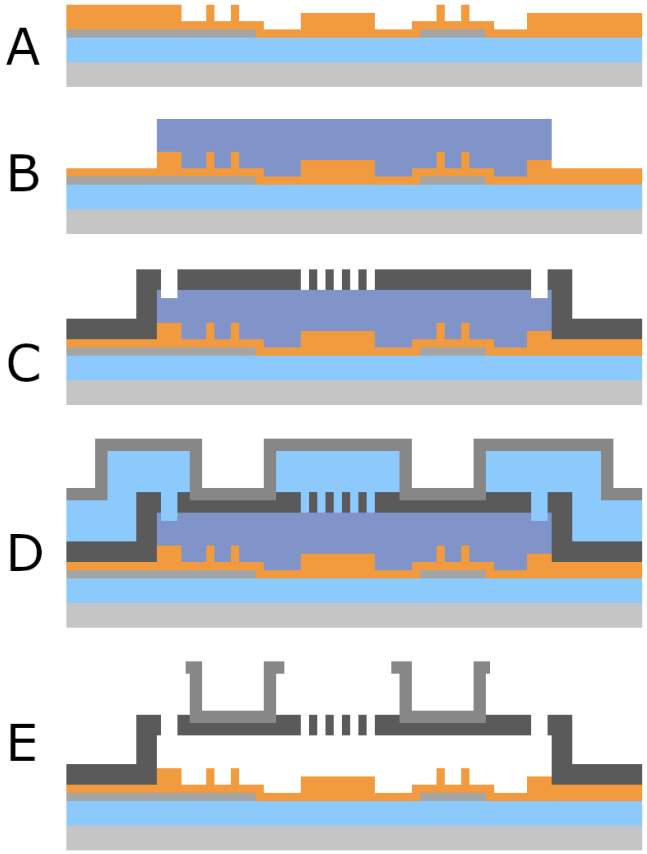

Fig. 3. Fabrication process for the optical switches.

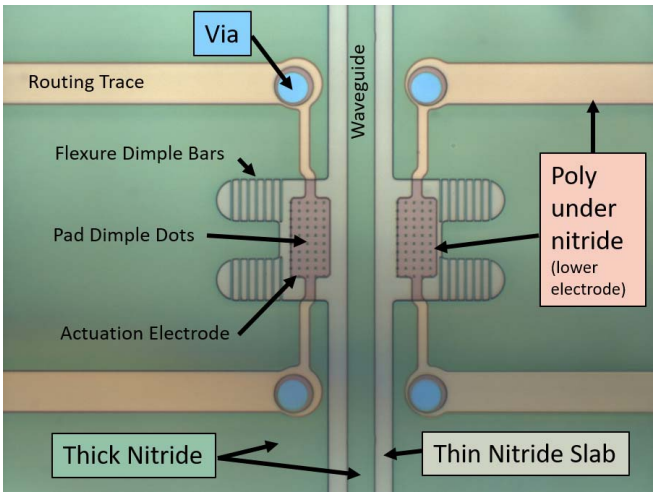

Fig. 4. Detail of waveguide and anti-stiction dimples, as shown by microscope image taken after the step shown in Figure 3A.

flexure locations (Fig. 4). These reduce the contact area and prevent the switch from sticking when pulled down ("ON" state.) The electrode thickness also sets the distance from the waveguide to the grating in the "ON" state, since the dimples are the same thickness as the waveguide. A 50 nm nitride slab is left in the etched areas to protect the lower cladding during release. At this stage, the device looks like Fig. 3A and Fig. 4.

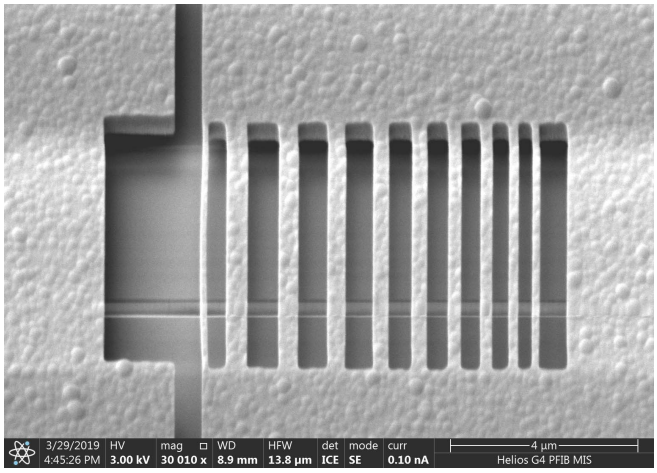

Fig. 5. Grating detail. Aperiodic gratings were designed to maximize efficiency while tailoring emission angle and numerical aperture. The horizontal waveguide is visible underneath.

Next, PECVD sacrificial oxide is deposited, planarized via CMP, and patterned, forming a sacrificial layer that will become the switch "OFF" state gap of 0.9 or 1.4 μm (Fig. 3B). Vias are etched through the oxide and nitride to provide electrical connections between the lower poly and the switch. The switch itself is constructed of 300 nm boron-doped polysilicon, etched (Fig. 3C) to form an optical grating (in the center) and supporting flexures (at the four corners). A detailed SEM of one grating design is shown in Fig. 5. The flexure dimensions are chosen to set the electrostatic pull-in voltage in the range of 5 to 40 Volts while being stiff enough to overcome stiction forces from the contact of the switch with the dimples.

The top of some switches is reinforced with an additional polysilicon layer deposited on the sidewall of another sacrificial oxide (Fig. 3D). This rib structure, etched in this 3rd polysilicon, stiffens the switch plate, to keep the grating geometry from deforming under actuation. At this stage, the wafer is diced, and the end facets of the waveguides are polished to improve coupling with the external optical fiber. The process is completed when the switches are released in HF followed by a critical point dry to prevent stiction (Fig. 3E). Throughout the process, contact lithography was used for features down to 1 μm, and e-beam lithography for smaller features.

III. Mechanical Performance

Switches were first tested by applying DC voltages to the actuation electrodes. Basic switches without the stiffening structures of Fig. 1 were tested first. A confocal laser microscope from Keyence was used to measure the deflection of the switch at each voltage with respect to the fixed anchor points, and example results are shown in Fig. 6. The deflection follows the classical MEMS formulae for non-linear electrostatic pull-in, including:

$$V_{\text{pull-in}} = \sqrt{\frac{8kg^3}{27\varepsilon A}}$$

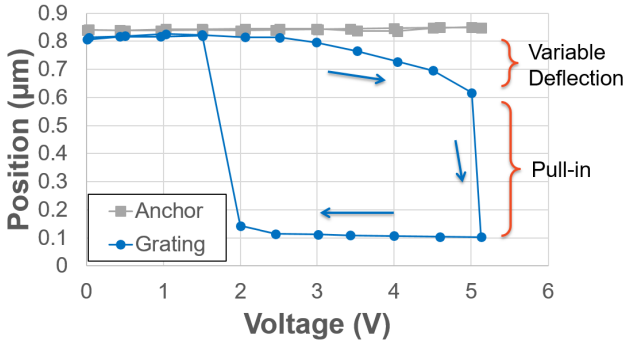

Fig. 6. Actuation of the switch at DC was measured with a laser confocal microscope. Deflection exhibits the classical non-linear electrostatic pull-in behavior. This switch had soft flexures, enabling pull-in at 5 V.

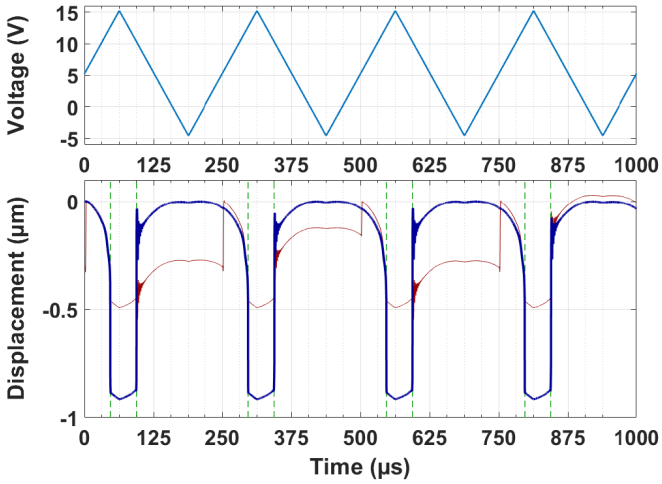

Fig. 7. Dynamic actuation of the switch at 4kHz in 40 Torr. The thin red trace is the raw output of the vibrometer. The raw output is corrected by offsetting each continuous portion of the trace in the ordinate to correct for tracking errors in the vibrometer system, yielding the thick blue trace.

and

$$z_{\text{pull-in}} = g/3$$

Pull-in actuators are used intentionally for this system because they provide the advantage of digital control. Pull-in to a specific hard stop location with well-defined optical performance is achieved despite variations in applied voltage, and the resulting beam position in the scene is determined by the location of the switch in the array. This contrasts with micro mirrors or optical phased arrays, where precise analog control of the mechanical gimbal or phase shifters is necessary to steer the beam across the scene.

Dynamic performance of the switches was also tested, using a Polytec MSA-400 laser Doppler vibrometer (LDV) system. This system uses an interferometer to measure velocity, and can also report displacements using a hardware integrator. Tests were performed at 40 Torr and atmospheric pressure. The system includes a function generator, which was used to apply sawtooth waveforms (Fig. 7) to the actuation electrodes to enable examination of behavior over many cycles. Sawtooth waveforms are convenient because their piecewise linear voltage vs. time segments show the nonlinear electrostatic

displacement behavior clearly. Actuation occurs with both positive and negative voltages, but we have usually biased the sawtooth drive signal, so that only one side results in pull-in.

The LDV system is not able to track the comparatively fast (<1 μs) motion during pull-in and release events. These show up as discontinuities in the raw output (red trace in Fig. 7) and as apparent offsets between successive "OFF" states (displacement $=$ 0). An additional discontinuity is caused when the hardware integrator resets, which is triggered on the rising zero-crossing of the sawtooth waveform before biasing (for example, at t=250, 500, 750 μs in Fig. 7). These erroneous discontinuities are removed by offsetting the continuous portion of the trace between them based on the known "ON" and "OFF" positions from DC measurement of the switch actuation.

Fig. 7 shows other details and non-idealities as well. First, partial actuation during the negative voltage cycle is visible as a cusp in the displacement (for example at t=188 μs). Also, the ringing of the switch at resonance after release can be seen as the switch returns to the "OFF" state each cycle. This results from low damping at 40 Torr; atmospheric pressure tests showed no ringing. Ringing never occurs at the "ON" position because the stop prevents it. Finally, the "ON" state (for example t=47 to 94 μs) is not flat, indicating that these original un-stiffened switches are not rigid, and continue to deform once part of them has made contact with the stop.

Many-cycle actuation showed that stiction correlates as expected to spring stiffness, and thus pull-in voltage. Switches with about 15V or higher pull-in reliably returned to the "OFF" state, while lower voltage designs sometimes stuck. For 300 μm^2 electrode area and 1 μm gap, this voltage threshold corresponds to a spring constant of about 2 N/m and a spring force in the "ON" state of 2 μN. This force is roughly equivalent to the stiction force, since devices that meet the stiffness and force threshold do not stick.

Devices which did not stick tended to last for many cycles. Fig. 9 shows six example devices, which were all connected to the function generator at 4kHz over about a month, with data collected periodically. This corresponded to over 9 billion cycles of actuation. For a typical frame rate of 30 Hz, 9 billion cycles corresponds to over 80,000 operational hours in a LiDAR system, well above automotive requirements. No degradation in switch performance was observed, indicating that the nitride dimples and polysilicon switch do not wear significantly. None of these switches failed after 9 billion cycles; the test was ended to free up the test equipment.

Actuation speed was also evaluated (Fig. 8). For actuation speed tests, a trapezoidal waveform was used, enabling the switch to fully settle in between ramped actuations. Switches were actuated as fast as 2-4 μs. At high speeds where the ramp approaches 10 μs, our drive amplifier was unable to maintain the shape of the waveform, and significant rounding of the trapezoid occurred. The fastest ramp the amplifier could supply was approximately 4 μs from 0 to 15 V. Likewise the LDV system is limited to 1 MHz sampling, so a different test apparatus would be needed to fully determine the ultimate switch speed limit for these devices. However, the switch times compare favorably with LiDAR requirements: round-trip

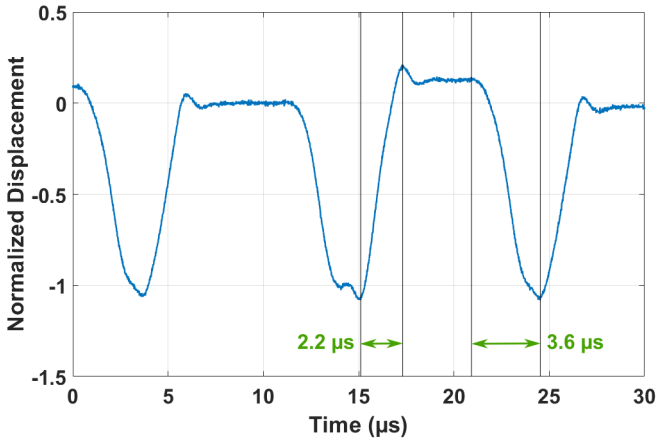

Fig. 8. Switching times of a few microseconds were demonstrated, sufficient for LiDAR frame rates and comparable to photon travel time. The "OFF" location varies because the vibrometer cannot track motion at this speed with no error; the displacement was normalized against known switch geometry.

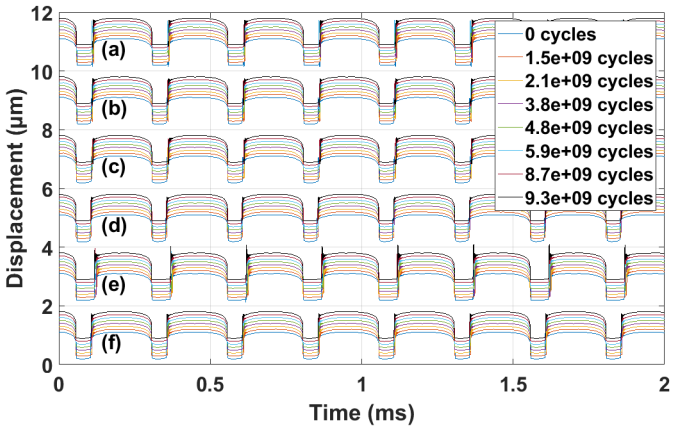

Fig. 9. Electrostatic actuation measured by LDV. Six switches, labeled (a) through (f), were tested. Switches were actuated 9 billion times, with no degradation. Curves are offset arbitrarily in the ordinate to show differences.

travel time for a photon to a range of 200 m is 1.33 μs, so switch times of order 1 μs prevent the switching time from dominating the system timing. Because the LDV system cannot track fast movements accurately, the amplitude of the speed test data in Fig. 8 is not reliable. To ensure we were fully actuating the switches, we started at lower speed so that the switch could be observed as stationary and therefore at the limit of its travel, and then gradually increased the speed, rather than relying on the displacement measurement. The displacements reported in Fig. 8 are then normalized, by dividing the traces by the average displacement difference between the stationary on and off periods, to eliminate the unreliable amplitude information.

Residual stress in the polysilicon was not a significant factor in switch deformation. We have used an optimized polysilicon deposition process, which deposits at 580°C and recrystallizes at 600°C. After doping and implant anneal, stress is typically measured at less than 100 MPa by wafer curvature. The resulting flatness of the suspended polysilicon structure is shown in Fig. 10.

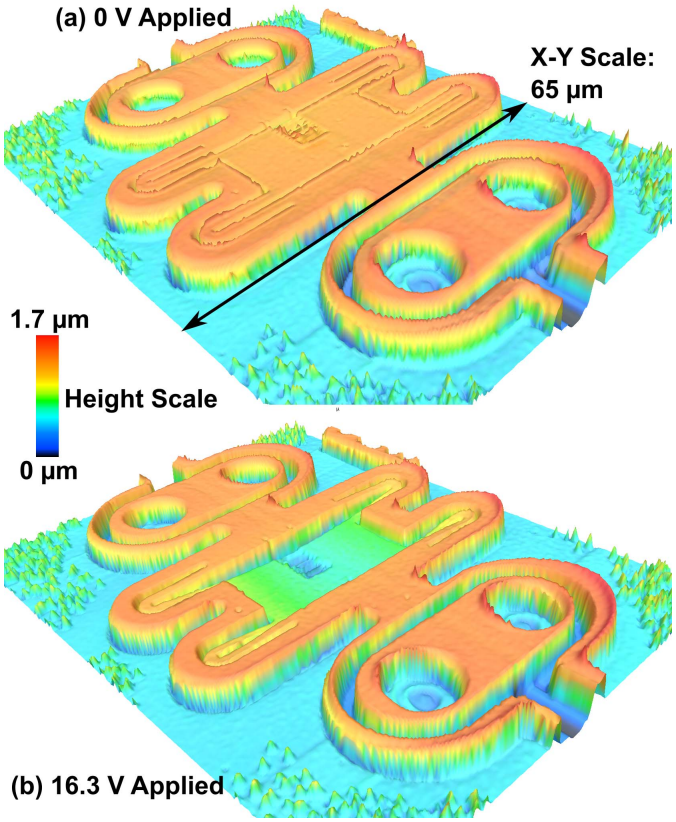

Fig. 10. The 3D structure of the unstiffened switch is measured. The "OFF" switch (a), with 0V applied, is flat, but the "ON" switch (b), with 16.3V applied, is deformed because of compliance in the electrode plate.

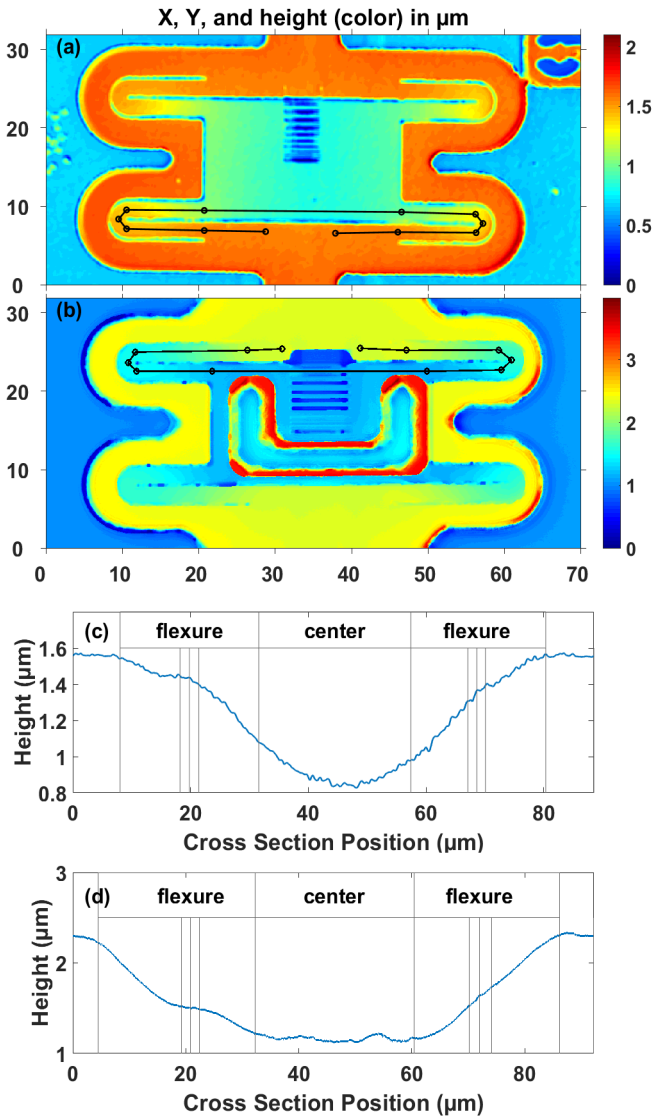

Fig. 11. Stiffeners greatly reduce bending of the electrode switch, including electrodes and grating. Image (a) shows the measured shape of an un-stiffened switch, pulled down at 16.3 V. (b) shows a stiffened switch, pulled down at 35 V. The higher voltage is needed because of the higher stiffness and larger electrostatic gap (1.5 μm instead of 1 μm). Multi-segment cross section locations are illustrated in black on (a) and (b). The cross section of the unstiffened switch (c) shows the center portion bows by 230 nm. In contrast, the stiffened switch (d) has a flatter shape with only 80 nm variation in the center portion, and 20 nm in the grating.

The most significant non-ideality in mechanical switch performance was bending of the central switch structure. Since the flexures and switch are fabricated in the same polysilicon layer, the bending stiffness of the central plate was similar to the flexures, and all parts deflected under actuation. This can be seen in the color variations of Fig. 10b and in the cross section measurement in Figure 11a&c. Deflections of 10s of nm can adversely affect the optical performance of the grating, since its critical features are sub-wavelength scale. The stiffener polysilicon (shown in Fig. 2) forms a flanged beam, greatly increasing stiffness of the plate, so deflections decreased from 230 nm to 30 nm (Fig. 11b&d).

IV. Optical Performance

Optical gratings were tested for performance [11]. In order to measure performance independent of switching characteristics, gratings without switches were first built directly on a 100 nm sacrificial oxide gap, simulating the position when pulled down. These gratings showed 73% optical efficiency, which compared well with the modeled efficiency of 75%. Grating emission patterns also matched the model well, as shown in Fig. 12.

Arrays of grating switches, as shown in Fig. 13, were used for LiDAR. This array comprises 10×10 switches, which form the focal plane of the LiDAR imaging system as illustrated in Fig. 1. A 1550 nm pulsed laser was connected via fiber to the edge of the waveguide. Electrostatic actuation of each switch pixel in sequence directed light out through a lens and aperture. The beam bounced off the target, and was directed by a mirror and lens into a single-photon avalanche diode (SPAD) for detection. The time for each beam pulse to return, divided by the speed of light, yields the range.

One advantage of the beam steering mechanism we demonstrate here is that a standard lens can be selected to map the focal plane array into the scene, with the desired parameters. The resolution of the received LiDAR image depends on the lens geometry and pixel spacing (100 μm in this case, though the switch could be patterned at pitches as small as 25 μm). For this demonstration, a lens was chosen which projects each pixel at a 0.1 degree spacing from each other.

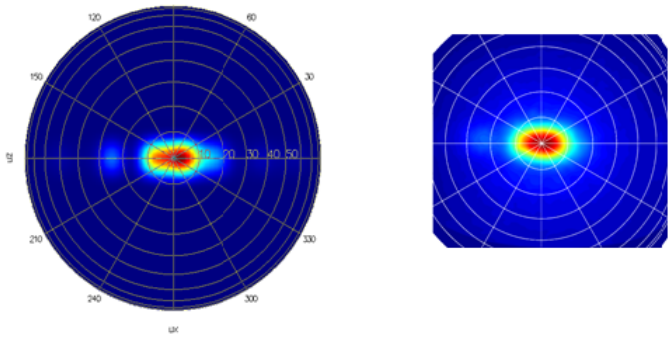

Fig. 12. Modeled grating emission patterns (left) matched experiment (right), for fixed gratings.

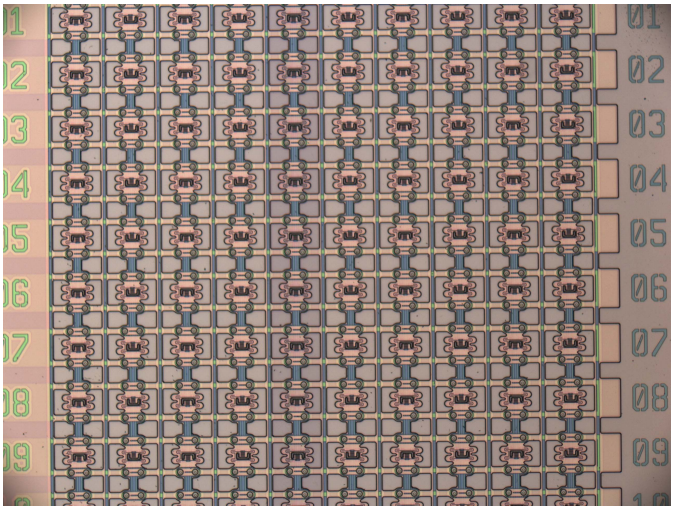

Fig. 13. Optical micrograph shows a fabricated array of 10 × 10 switches. This array serves as the focal plane of a LiDAR device, projecting light from the selected pixel into the optics.

This horizontal and vertical resolution was chosen based on requirements from automotive LiDAR systems. With 10 pixels that leads to a 1 degree field of view (FOV). Assuming a 10 μs dwell per pixel, a similar LiDAR system could scan 100,000 pixels/s, such as in a 4 degree by 10 degree FOV with 0.1 degree resolution at 25 frames/sec. For larger FOV with comparable resolution, multiple laser and detector pairs can serve subarrays concurrently, or random-access scanning algorithms can prioritize scanning of pixels that contain important information.

Range resolution for this type of LiDAR system depends in large part on the pulse width of the laser, and is independent of the beam steering mechanism we present here. We have used a laser with a pulse width of about 1 ns, leading to a range resolution of half the light travel distance in that time, or about 15 cm. Other contributions come from the jitter in laser pulse timing, and the detector time resolution, but those are both much smaller than 1 ns in our setup. The range resolution could be improved by averaging over several returns, but we have not done that in this case, since the focus of the work is on the beam steering system. An example LiDAR data point cloud gathered by this demonstration hardware is shown in Fig. 14.

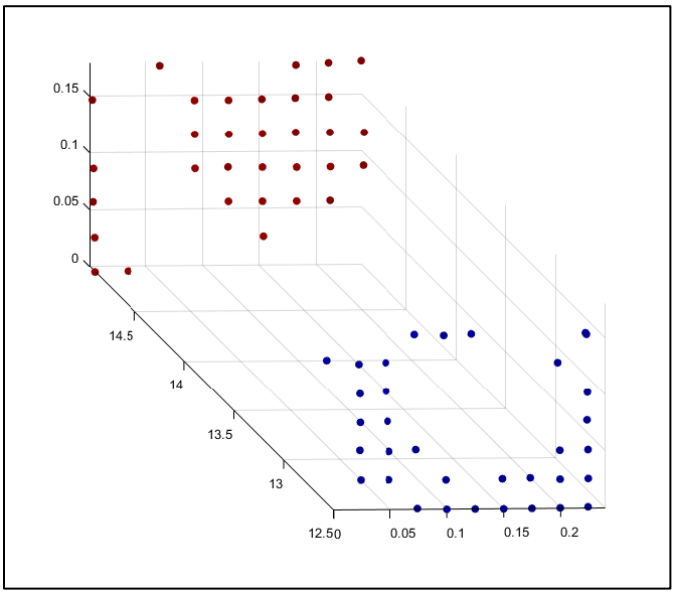

Fig. 14. LiDAR point cloud collected using a grating switch array. Axis units are meters. The foreground (blue points) reflected off a toroidal target, in front of a wall (red points).

This image shows full functionality of the LiDAR system, in returning a 3D image from the scene. It should be noted that a defect in this device prevented much of the light from reaching the last 3 rows of gratings, and there is no LiDAR from these rows. However, the grating switches in these rows otherwise functioned properly.

REFERENCES

[1] C. Ilas, "Electronic sensing technologies for autonomous ground vehicles: A review," in *Proc. 8TH Int. Symp. Adv. TOPICS Electr. Eng. (ATEE)*, Bucharest, Romania, May 2013, pp. 1–6.

[2] E. Yurtsever, J. Lambert, A. Carballo, and K. Takeda, "A survey of autonomous driving: Common practices and emerging technologies," *IEEE Access*, vol. 8, pp. 58443–58469, 2020, doi: 10.1109/ACCESS.2020.2983149.

[3] C. V. Poulton *et al.*, "Coherent solid-state LIDAR with silicon photonic optical phased arrays," *Opt. Lett.*, vol. 42, no. 20, p. 4091, Oct. 2017, doi: 10.1364/OL.42.004091.

[4] S. A. Miller *et al.*, "512-element actively steered silicon phased array for low-power LIDAR," in *Proc. Conf. Lasers Electro-Opt.*, San Hose, CA, USA, 2018, Paper JTh5C-2, doi: 10.1364/CLEO_AT.2018.JTh5C.2.

[5] P. F. Mcmanamon, P. Banks, J. Beck, D. G. Fried, A. S. Huntington, and E. A. Watson, "Comparison of flash lidar detector options," *Opt. Eng.*, vol. 56, no. 3, Mar. 2017, Art. no. 031223, doi: 10.1117/1.OE.56.3.031223.

[6] A. Kasturi *et al.*, "Comparison of MEMS mirror LiDAR architectures," *Proc. SPIE MOEMS Miniaturized Syst.*, vol. 11293, Feb. 2020, Art. no. 112930B.

[7] J. J. López *et al.*, "Planar-lens enabled beam steering for chip-scale LIDAR," in *Proc. Conf. Lasers Electro-Opt.*, 2018. San Jose, CA, 2018, Paper SM3I.1.

[8] C. Li, X. Cao, K. Wu, X. Li, and J. Chen, "A switch-based integrated 2D beam-steering device for lidar application," in *Proc. Conf. Lasers Electro-Opt.*, San Jose, CA, 2019, Paper JTh2A.

[9] T. J. Seok, N. Quack, S. Han, R. S. Muller, and M. C. Wu, "Large-scale broadband digital silicon photonic switches with vertical adiabatic couplers," *Optica*, vol. 3, no. 1, pp. 64–70, Jan. 2016.

[10] X. Zhang, K. Kwon, J. Henriksson, J. Luo, and M. C. Wu, "20×20 focal plane switch array for optical beam steering," in *Proc. Conf. Lasers Electro-Opt. (CLEO)*, San Jose, CA, USA, 2020.

[11] S. J. Spector *et al.*, "LiDAR beamsteering by digitally switched MEMS gratings on a silicon photonics platform," in *Proc. Conf. Lasers Electro-Opt. (CLEO)*, San Jose, CA, USA, 2020.